

Article

Oxidation Performance of Nano-Layered (AlTiZrHfTa) N_x /Si N_x Coatings Deposited by Reactive Magnetron Sputtering

Djallel Eddine Touaibia ^{1,2,*} , Sofiane Achache ^{1,2}, Abdelhakim Bouissil ^{1,2}, Fabrice Parent ^{1,2}, Jaafar Ghanbaja ³, Alina Gorbunova ⁴ , Pavel S. Postnikov ⁴ , Mohamed Mehdi Chehimi ⁵ , Frederic Schuster ⁶, Frederic Sanchette ^{1,2}  and Mohamed El Garah ^{1,2,*} 

¹ LASMIS—Laboratory of Mechanical & Materials Engineering, Antenne de Nogent-52, Pôle Technologique de Sud-Champagne, 52800 Nogent, France; soufyane.achache@utt.fr (S.A.); abdelhakim.bouissil@utt.fr (A.B.); fabrice.parent@utt.fr (F.P.); frederic.sanchette@utt.fr (F.S.)

² LRC CEA-LASMIS, Nogent International Centre for Coating Innovation (NICCI), Pôle Technologique de Sud-Champagne, 52800 Nogent, France

³ Institut Jean Lamour (UMR CRS 7198), Université de Lorraine, 54000 Nancy, France; jaafar.ghanbaja@univ-lorraine.fr

⁴ Research School of Chemistry and Applied Biomedical Sciences, Tomsk Polytechnic University, Tomsk 634050, Russia; aag84@tpu.ru (A.G.); pavelpostnikov@gmail.com (P.S.P.)

⁵ ITODYS, CNRS, UMR 7086, University of Paris, 15 rue JA de Baïf, 75013 Paris, France; mmchehimi@yahoo.fr

⁶ Commissariat à l’Energie Atomique et aux énergies Alternatives (CEA) Saclay, 91191 Gif-sur Yvette, France; frederic.schuster@cea.fr

* Correspondence: djallel_eddine.touaibia@utt.fr (D.E.T.); mohamed.el_garah@utt.fr (M.E.G.)

Abstract: This work uses the direct current magnetron sputtering (DCMS) of equi-atomic (AlTiZrHfTa) and Si targets in dynamic sweep mode to deposit nano-layered (AlTiZrHfTa) N_x /Si N_x refractory high-entropy coatings (RHECs). Transmission electron microscopy (TEM), field emission scanning electron microscopy (FESEM), thermogravimetric analysis (TGA), X-ray diffraction (XRD), and X-ray photoelectron spectroscopy (XPS) are used to investigate the effect of Si addition on the oxidation behavior of the nano-layered coatings. The Si-free nitride coating exhibits FCC structure and columnar morphology, while the Si-doped nitride coatings present a FCC (AlTiZrHfTa) N_x /amorphous-Si N_x nano-layered architecture. The hardness decreases from 24.3 ± 1.0 GPa to 17.5 ± 1.0 GPa because of the nano-layered architecture, whilst Young’s modulus reduces from 188.0 ± 1.0 GPa to roughly 162.4 ± 1.0 GPa. By increasing the thickness of the Si N_x nano-layer, k_p values decrease significantly from $3.36 \times 10^{-8} \text{ g}^2 \text{ cm}^{-4} \text{ h}^{-1}$ to $6.06 \times 10^{-9} \text{ g}^2 \text{ cm}^{-4} \text{ h}^{-1}$. The activation energy increases from $90.8 \text{ kJ} \cdot \text{mol}^{-1}$ for (AlTiZrHfTa) N_x nitride coating to $126.52 \text{ kJ} \cdot \text{mol}^{-1}$ for the (AlTiZrHfTa) N_x /Si N_x nano-layered coating. The formation of a FCC (AlTiZrHfTa)- N_x /a-Si N_x nano-layered architecture results in the improvement of the resistance to oxidation at high temperature.

Keywords: high-entropy alloys; coatings; magnetron sputtering; (AlTiZrHfTa)/Si N_x ; oxidation; nano-layered



Citation: Touaibia, D.E.; Achache, S.; Bouissil, A.; Parent, F.; Ghanbaja, J.; Gorbunova, A.; Postnikov, P.S.; Chehimi, M.M.; Schuster, F.; Sanchette, F.; et al. Oxidation Performance of Nano-Layered (AlTiZrHfTa) N_x /Si N_x Coatings Deposited by Reactive Magnetron Sputtering. *Materials* **2024**, *17*, 2799. <https://doi.org/10.3390/ma17122799>

Academic Editors: Liuquan Yang, Hao Du and Rui Shu

Received: 7 May 2024

Revised: 1 June 2024

Accepted: 4 June 2024

Published: 7 June 2024



Copyright: © 2024 by the authors. Licensee MDPI, Basel, Switzerland. This article is an open access article distributed under the terms and conditions of the Creative Commons Attribution (CC BY) license (<https://creativecommons.org/licenses/by/4.0/>).

1. Introduction

The expanding strives for innovative materials—required to operate in demanding thermal and mechanical environments in industry—leads to several initiatives in academia and industry. The most crucial characteristics needed for protective coatings are high hardness, strong adherence to surfaces, high strength at high temperatures, and good oxidation resistance [1,2]. This is why innovative coatings with increased hardness, wear, and oxidation resistance are urgently required and should be studied. Binary system coatings such as TiN and CrN [3], ternary coatings such as CrAlN [4,5], multilayer coatings such as TiC/VC [6], TiAlN/CrN [7], TiN/Si $_3$ N $_4$ [8], and other multilayer nano-composite coatings [9–11] have all been steadily investigated and used extensively. Multilayers showed interesting properties in terms of hardness, wear, and oxidation resistances [12–16].

The alloying concept of high-entropy alloys (HEAs), or multi-principal-element alloys, is believed to hold promise in this regard. Generally, HEAs are formed of at least five elements with atomic ratios varying from 5 to 35 at.%, characterized by a single-phased solid solution [17,18]. They have a high mixing entropy compared to conventional alloys in the solution state, allowing them to form stable solid solutions at high temperatures and inhibiting the formation of undesired brittle intermetallic compounds [19–21]. Hence, HEAs are considered as a potential class of materials for protective coatings [22–25].

Refractory high-entropy alloys (RHEAs) based on transition group metals have interesting applications in several devices [8,26,27]. However, they frequently exhibit room-temperature brittleness and poor oxidation resistance at elevated temperatures [28–31]. Several studies have been undertaken in the past to improve the oxidation resistance of refractory alloys through alloying additions containing metals such as Al, Cr, and Si. When introduced in an appropriate amount, these elements may stimulate the formation of protective oxide top-layers like: Al_2O_3 , Cr_2O_3 , and SiO_2 [29,32–34].

The critical challenge for RHEAs is still high-temperature oxidation resistance. Muller et al. [35] enhanced the protective properties of TaMoCrTiAl RHEAs by alloying with Cr and Al. The combination of Al and Cr resulted in the development of adhering and protective CrTaO_4 oxide scale. The CrTaO_4 layer was formed in the 500–1200 °C temperature range. Sheikh et al. [29] performed an aluminizing process on the ductile $\text{Al}_{0.5}\text{Cr}_{0.5}\text{Nb}_{0.5}\text{Ta}_{0.5}\text{Ti}_{0.5}$. They reported an improvement in the oxidation resistance of the coating at 800 °C.

According to the literature, adding silicon increases oxidation resistance at high temperatures [24,36]. Yu et al. [24] used magnetron sputtering technology to deposit (AlCrTiZrMo)- Si_x -N coatings with varying silicon contents and investigated its effect on the structure and properties of the coatings. The addition of silicon resulted in grain refinement of the microstructure due to the formation of nano-composite architecture (FCC (AlCrTiZrMo)N nano-crystallites encapsulated by the amorphous Si_3N_4 phases). Due to the increase in Si content in the coating, high hardness, and Young's modulus were achieved at 28.5 GPa and 325.4 GPa, respectively. When the Si content exceeds 4.5 at.%, the hardness and Young's modulus decreased, due to an excess of amorphous boundary phase in the coating.

Different multilayered coatings, such as (TiZrNbTaHf)N/MoN [37], (TiZrNbTaHf)N/WN [38] prepared by vacuum-arc deposition, AlCrRuTaTiZr/(AlCrRuTaTiZr)N [25] and AlCrMoNbZr/(AlCrMoNbZr)N [39,40], deposited by reactive magnetron sputtering, were investigated. They exhibit good corrosion resistance, interface stability and mechanical properties. These multi-layer high-entropy nitride ceramic coatings (HENCFCs) offer tunable features and promise for use in tool coating materials [41].

The aim of this study is to depict the Si and the nano-layered architecture effects on the oxidation resistance enhancement of the (AlTiZrHfTa) N_x RHEC, obtained at $R_{\text{N}_2} = 10\%$ with ($R_{\text{N}_2} = \text{N}_2 / (\text{Ar} + \text{N}_2)$). In fact, this work is performed in line with the previous study with a deep focus on (AlTiZrHfTa) N_x RHECs and the improvement of their oxidation resistance [42]. The FCC (AlTiZrHfTa) N_x /a-Si N_x nano-layered coatings were deposited by reactive DCMS of equi-atomic (AlTiZrHfTa) and Si targets in dynamic sweep mode, to provide adjustable coating characteristics [43]. Furthermore, the microstructure evolution, the chemical composition, the structure, and the mechanical properties are also addressed.

2. Materials and Methods

2.1. Deposition of the Coatings

The FCC (AlTiZrHfTa) N_x /a-Si N_x RHECs were deposited by means of DP 650 Alliance Concept device (. The RHECs were deposited on different substrates: flat glass for X-ray diffraction (XRD) analysis, on Si (100) for scanning electron microscopy (SEM), electron probe micro-analysis (EPMA), and transmission electron microscopy (TEM) investigations, and (0 0 0 1)-oriented sapphires substrates for TGA. The co-deposition was carried out by reactive DCMS of 99.99% pure equi-atomic (AlTiZrHfTa) HEA and 99.99% (brazed)

Si targets. Prior to loading into the reactor, the substrates were ultrasonically cleaned in acetone and ethanol. The distance between the targets and the substrate holder was 6 cm.

Before deposition, the targets were homogeneously sputtered by argon ions for 10 min at (1 Pa). Afterwards, the substrates' surfaces were etched with argon ions (1 Pa) by RF power of 200 watts for a during 23 min. The HEA target current intensity was 1.0 A; however, the current intensity of Si target (I_{Si}) varied from 0 A to 0.4 A. The coatings were deposited, at 1 Pa, under R_{N_2} flow ratios of 10%. During deposition, a rotating substrate holder was used (rotating speed = 2 rpm), with a sweep mode (amplitude = 180°), Figure 1. The deposition durations were adjusted to obtain at least $2\ \mu\text{m}$ -thickness for all coatings.

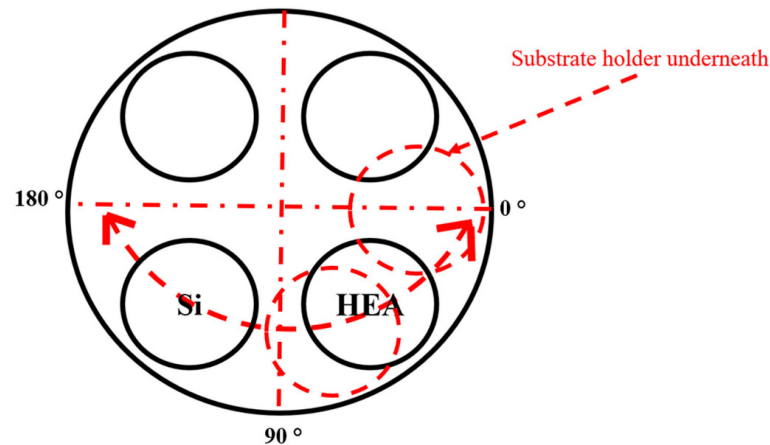


Figure 1. Targets disposition inside the reactor.

2.2. Sample Analysis

2.2.1. Structure and Microstructure Characterization

The crystal phase identification was carried out by X-ray diffraction on the D8-Advance Bruker diffractometer (Bruker, Billerica, MA, USA) in Bragg–Brentano symmetrical mode, with a radiation source of $\text{Cu K}\alpha$ ($\lambda = 1.544184\ \text{\AA}$, 40 kV, 40 mA), a scanning range of 20° to 100° with a step speed of $0.02^\circ/\text{s}$. TEM studies of the coatings were carried out by using a JEM-ARM 200F cold Field Emission Gun (FEG) (JEOL, Tokyo, Japan) (TEM/Scanning Transmission Electron Microscopy STEM). The TEM instrument was running at 200 kV and equipped with an image corrector and a spherical aberration (Cs) probe (point resolution 0.12 nm in TEM mode and 0.078 nm in STEM mode). Focused Ion Beam/Scanning Electron Microscopy (FIB/SEM) FEI Helios NanoLab 600i (FEI, Hillsboro, OR, USA) with platinum Gas Injection System was used to prepare TEM samples. The chemical compositions of the $(\text{AlTiZrHfTa})\text{N}_x/\text{a-SiN}_x$ RHECs were analyzed using EPMA (microprobe JEOL JXA-8530F, JEOL, Tokyo, Japan). The bonding structure of the nano-layered coatings was characterized by X-ray photoelectron spectroscopy using an NEXSA apparatus (Thermo, East Grinstead, UK) fitted with a monochromatic X-ray $\text{Al K}\alpha$ source (energy = 1486.6 eV and power = 150 W).

A TESCAN MIRA Field emission source electron–Schottky electron gun was used to measure the thickness and examine the morphology of the coatings' cross-sections and surfaces.

2.2.2. Mechanical Properties

The deposited high-entropy coatings' nano-hardness (H) and reduced Young's modulus (ER) were measured by using a HYSITRON, TI980 Triboindenter instrument (Bruker Nano, Inc, Eden Prairie, MN, USA) equipped with a Berkovitch indenter (Bruker Nano, Inc, Eden Prairie, MN, USA). To eliminate the effects of substrate stiffness, the maximum penetration depth is set to less than 10% of the coating thickness. The values of hardness and Young's modulus were calculated by taking an average of thirty indents.

2.2.3. High-Temperature Oxidation Tests

A thermogravimetric analyzer (TGA, SETARAM, SETSYS evolution, (SETARAM Instrumentation KEP Technologies, Caluire-et-Cuire, France) was used to conduct the oxidation tests in a dry-air (80% N₂, 20% O₂) atmosphere. The (0 0 0 1)-oriented sapphires were dual-side coated and served as the test specimens for the TGA. Two different testing protocols were utilized: the first was dynamic and the second protocol was static; more details are provided in reference [42]. Both protocols are used to evaluate the oxidation resistance of the coatings and assess the effect of Si addition on the oxidation performances of the RHECs.

3. Results and Discussion

3.1. Microstructure of (AlTiZrHfTa)N_x/SiN_x Thin Coatings

TEM investigations were performed on the selected samples of (AlTiZrHfTa)N_x nitride coating and high-entropy nitride coating obtained for I_{Si} = 0.2 A. This latter coating presented a protective one of the best oxidation behavior (Section 3.6.2). Figure 2 presents the cross-sectional TEM bright field micrographs, and the selected area presents electron diffraction (SAED) patterns of the FCC (AlTiZrHfTa)N_x/amorphous SiN_x obtained for I_{Si} = 0.2 A. The HRTEM (high-resolution transmission electron microscopy) micrograph and compositional profile of (AlTiZrHfTa)N_x RHECs obtained for I_{Si} = 0.2 A are also shown.

In the previous study [42], the results showed that the (AlTiZrHfTa)N_x nitride coating exhibits a stable FCC-single phased structure. In addition, the nitride coating features a coarse, fiber-like grain structure in the coating growth, as well as a V-shaped growth of faceted columns, indicating T zone pattern growth (Barna Model) [44]. (AlTiZrHfTa)N_x nitride presented a monolithic architecture.

When (AlTiZrHfTa)N_x/SiN_x is deposited, the coating is denser (Figure 2a) compared to the (AlTiZrHfTa)N_x nitride coating, which has a columnar morphology [42]. For (AlTiZrHfTa)N_x/SiN_x coating, obtained at I_{Si} = 0.2 A, an obvious nano-layered structure was observed with clear interfaces between the Si–N nano-layer and (AlTiZrHfTa)N_x nano-layer (Figure 2b,c). The period $\alpha = t(\text{AlTiZrHfTa})\text{N}_x + t\text{SiN}_x$ layer, where $t(\text{AlTiZrHfTa})\text{N}_x$ and $t\text{SiN}_x$ are the thicknesses of the (AlTiZrHfTa)-N_x nano-layer and the SiN_x nano-layer, was measured at around 5 nm with $t_{(\text{AlTiZrHfTa})\text{N}_x}$ layer = 3.5 nm, and t_{SiN_x} layer = 1.5 nm (Figure 2c). A similar configuration was observed by Cai et al. [45] and Xu et al. [46] when investigating dual phase CoCrCuFeNi/Al nano-layered and TiAlN/TiN, TiAlN/ZrN nano-layered coatings, respectively. In our case, the nano-layered architecture is formed with a thinner period. During the process, the small target–substrate distance (6 cm) and a low sweep rate (2 rpm) made the substrates become exposed separately, for a certain duration, to each target.

The HRTEM image shows the presence of a nano-layered structure (Figure 2c). The SAED pattern, presented in Figure 2d, reveals that the SiN_x nano-layer is amorphous and the (AlTiZrHfTa)N_x nano-layer is a clear FCC crystalline structure (Figure 2d). Furthermore, line-scan EDS profiles, illustrated in Figure 2e,f indicate clearly the presence of fluctuations in Si and (Al,Ti,Zr,Hf,Ta) concentrations between neighboring nano-layers, as well as a relatively stable N concentration profile. These indicate that (1) all elements are bounded with nitrogen and (2) the multilayer exists at nano-metric scale ((AlTiZrHfTa)N_x + SiN_x).

The XPS technology has been used to identify the different bonding between the constituent elements of the RHECs. Our group has published the XPS spectra, where the full spectrum was shown, of the (AlTiZrHfTa)N_x coating for various nitrogen flow rates (R_{N2}) [47,48]. In this work, we proceeded with the silicon bounding only and the results are presented in Figure 3. The Si 2p spectrum shows the presence of one peak at 101.8 eV that can be assigned to Si–N bonds in SiN_x. Similar trend have been reported by Shi et al. [49] and Yu et al. [24], revealing the formation of a Si₃N₄ component. As the I_{Si} increases, the thickness of the SiN_x layer increases.

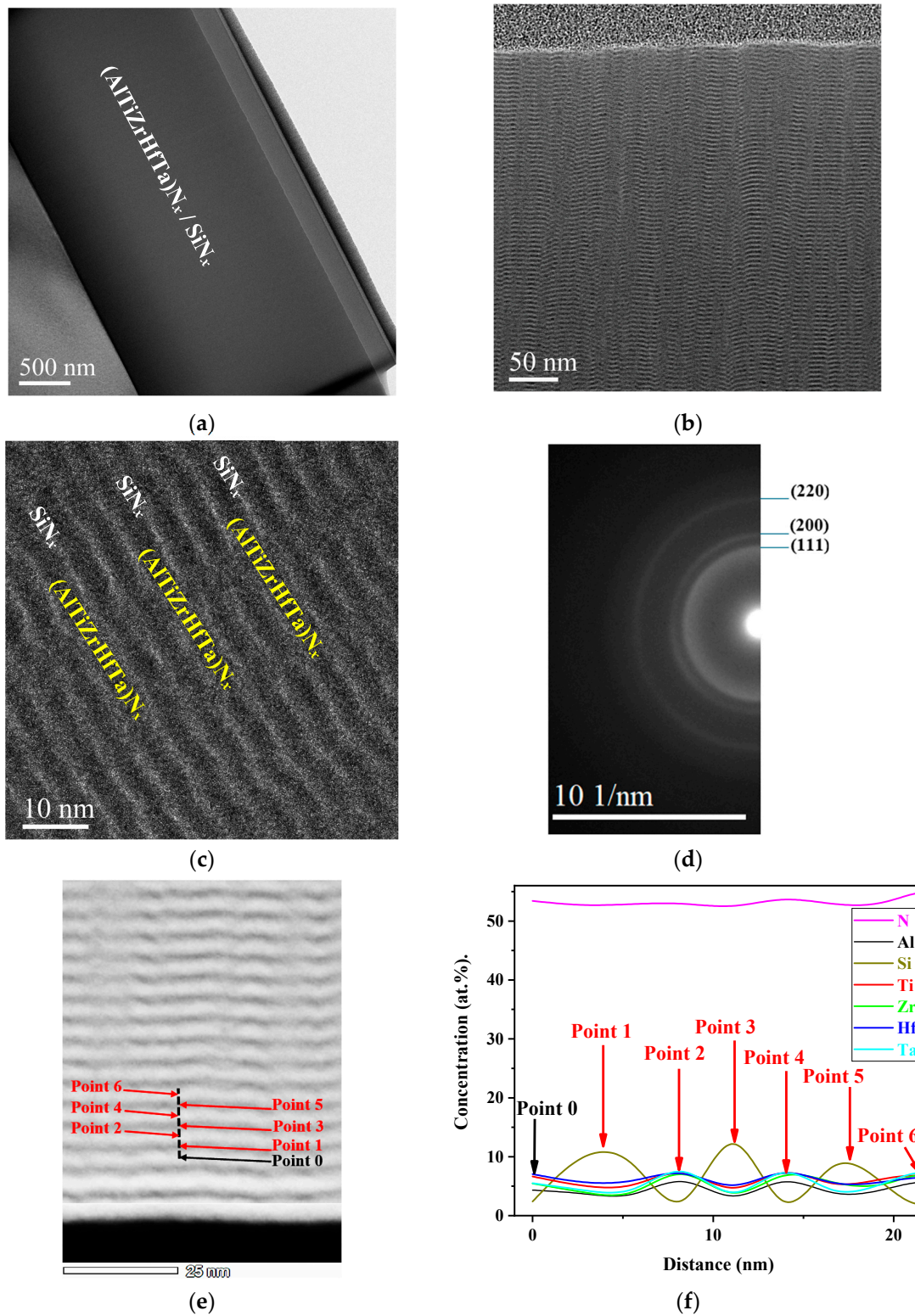


Figure 2. (a) Bright field micrograph of the $(AlTiZrHfTa)_x/Si_x$ coating at $R_{N_2} = 10\%$ obtained for $I_{Si} = 0.2$ A. (b) Zoom-in on nano-layered FCC $(AlTiZrHfTa)_x/a-Si_x$. (c) HRTEM micrograph. (d) SAED pattern of the FCC $(AlTiZrHfTa)_x/Si_x$ coating obtained for $I_{Si} = 0.2$ A. (e) STEM HAADF image of the FCC $(AlTiZrHfTa)_x/Si_x$ coating obtained for $I_{Si} = 0.2$ A, showing the scan line of nano-probe EDX and (f) compositional profiles across the nano-layered thin coating.

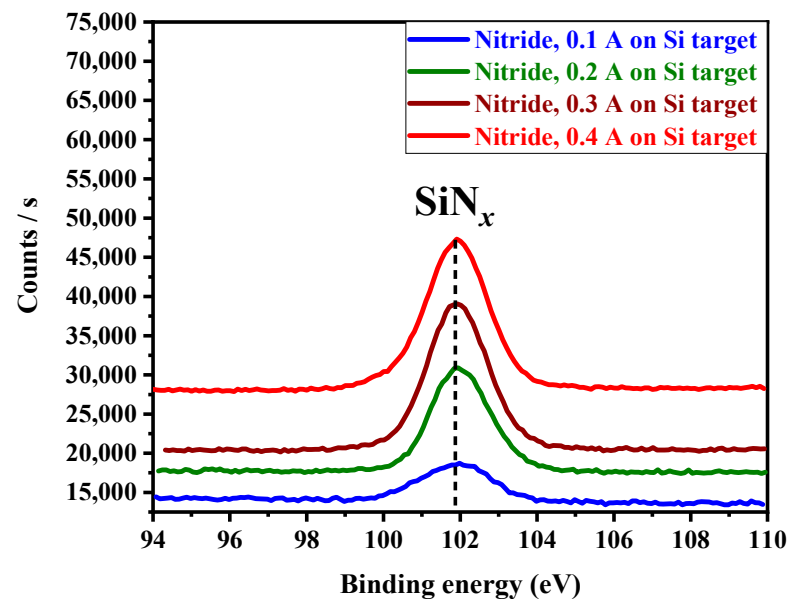


Figure 3. Si 2p XPS spectrum of (AlTiZrHfTa)-N_x/SiN_x nitride coatings as a function of I_{Si}.

3.2. Structure and Microstructure

Figure 4 illustrates the XRD patterns of FCC (AlTiZrHfTa)N_x/a-SiN_x RHECs as a function of I_{Si}, for R_{N2} = 10%. The diffraction peaks were identified to TaN structure (CIF No. 2310957). The (AlTiZrHfTa)N_x (R_{N2} = 10%) nitride coating exhibits single-phased [NaCl-type (β1)] FCC solid solution structure (Figure 4a), rather than any complex phase separations [50–52]. This trend has been figured out in the previous studies [42,48] and observed in the literature as well, for several high-entropy thin coatings like: AlCrTaTiZr [52], AlCrMoSiTi [53], TiVCrZrHf [54], and TiTaZrHfW [55].

When (AlTiZrHfTa)N_x/SiN_x coatings are deposited, XRD patterns (Figure 4b) show low-intensity and large diffraction peaks (Figure 4b), compared to that of nitride, which is directly linked to the formation the nano-layered architecture, alternating FCC (AlTiZrHfTa)N_x nano-layers and amorphous SiN_x nano-layers as shown in (Section 3.1). In fact, the SiN_x-based compound presents an amorphous aspect [8,50,56,57] and inhibits the growth of the nitride columns [8,58], resulting in the broadening of the peaks when depositing (AlTiZrHfTa)N_x/SiN_x.

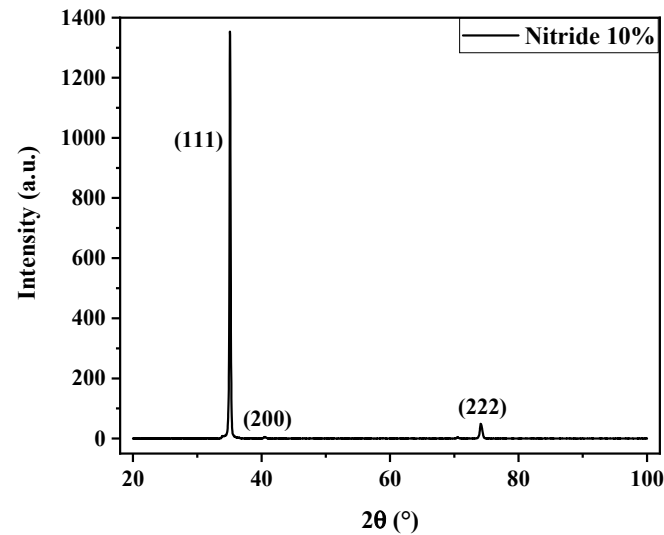
The average grain size (Ø) is calculated from the most intense (111) peaks, by using the Scherrer equation [59]. The mean grain size values decreased from 45.92 nm for FCC (AlTiZrHfTa)-N_x coating to ~2 nm for all the FCC (AlTiZrHfTa)-N_x/a-SiN_x coatings (Table 1).

Table 1. The calculated mean grain size values, measured by the Scherrer equation, of the FCC (AlTiZrHfTa)N/a-SiN_x coatings as a function of I_{Si}.

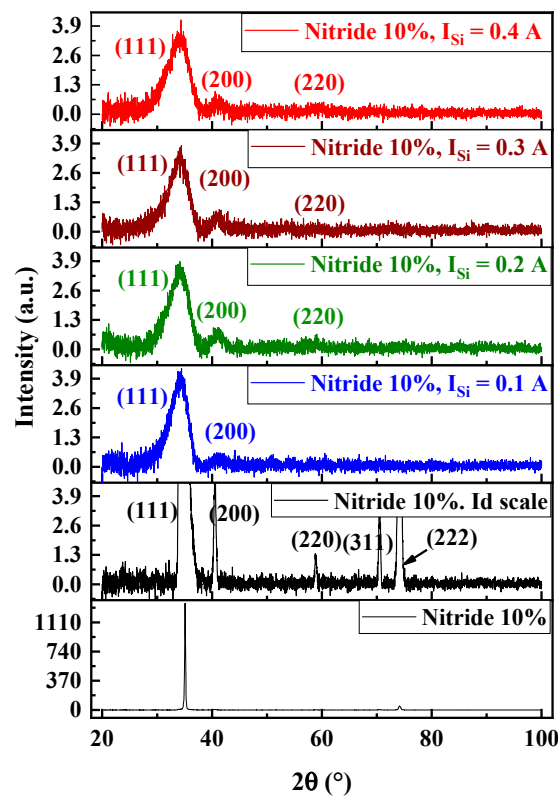
Coating	I _{Si} (A)	Average Grain Size, Ø (nm)
(AlTiZrHfTa)N (R _{N2} = 10%)	0	45.92
(AlTiZrHfTa)N _x /SiN _x (R _{N2} = 10%)	0.1	2.1
(AlTiZrHfTa)N _x /SiN _x (R _{N2} = 10%)	0.2	2
(AlTiZrHfTa)N _x /SiN _x (R _{N2} = 10%)	0.3	2
(AlTiZrHfTa)N _x /SiN _x (R _{N2} = 10%)	0.4	2.2

However, according to the comprehensive research so far, at room temperature, refractory metal nitrides deposited on substrates require some time to achieve a high-crystalline structure [42,54,55,60]. Nieborek et al. [61] observed that the grain size of the magnetron sputtered TiN increases as the coating grows. They clearly showed (Figure 7d in reference [61]) that at the interface between TiN film and the substrate, the coating is almost

amorphous. The grains with small size (almost amorphous) can be found at the interface with the substrate, and as the coating becomes thicker, the grain size increases, reaching its maximum near the surface. In this study, the deposition of SiN_x resumes crystallization and renders all layers nearly amorphous. That is why there is a direct drop in the average grain size after the introduction of the SiN_x layer and no dependence on the SiN_x layer thickness (Table 1). The further increase in I_{Si} could lead to the increase in the deposition rate, which leads to the increase in the thickness of the SiN_x nano-layer.



(a)



(b)

Figure 4. X-ray diffraction patterns of (a) Si-free $(\text{AlTiZrHfTa})\text{N}_x$ nitride coating and (b) FCC $(\text{AlTiZrHfTa})\text{N}_x/\text{a-SiN}_x$ coatings as a function of I_{Si} .

3.3. Morphology of FCC (AlTiZrHfTa) N_x/a -Si N_x Thin Coatings

The cross-sectional and top view SEM micrographs of the FCC (AlTiZrHfTa) N_x/a -Si N_x RHECs with various I_{Si} are shown in Figure 5. As we can notice from the figure, the coatings have a good combination with the silicon substrate. No obvious defects have been observed.

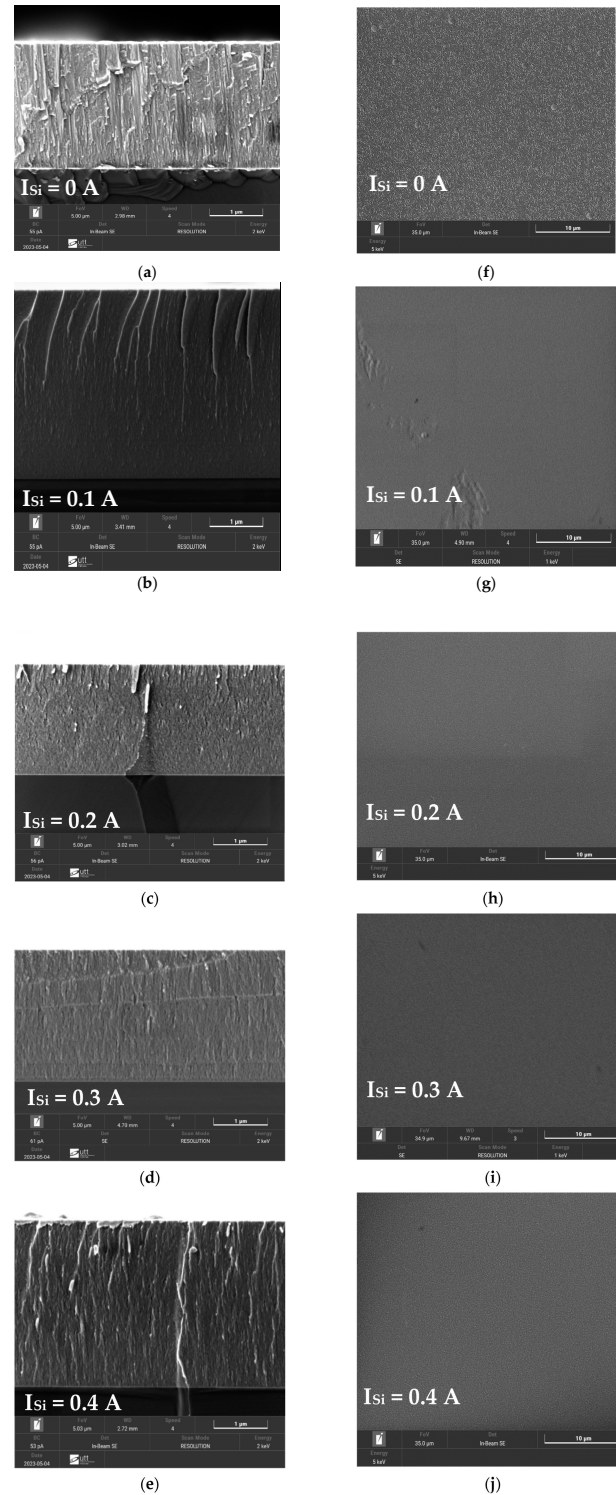


Figure 5. Cross-sectional (left images) and surface SEM morphologies (right images) of (AlTiZrHfTa) N_x /Si N_x RHECs for $R_{N2} = 10\%$ obtained for (a,f) $I_{Si} = 0$ A, (b,g) $I_{Si} = 0.1$ A, (c,h) $I_{Si} = 0.2$ A, (d,i) $I_{Si} = 0.3$ A, and (e,j) $I_{Si} = 0.4$ A.

For the (AlTiZrHfTa) N_x nitride coating (Figure 5a), large columnar morphology throughout the coating is observed, while the surface presents a pyramid-like aspect (Figure 5f). However, when FCC (AlTiZrHfTa) N_x /a-Si N_x is deposited, the coatings exhibit a dense, smooth cross-sectional morphology and no obvious columnar growth (Figure 5b–e). This aspect is linked to the formed nano-layered architecture, illustrated in Figure 2b, during the coating growth. As illustrated in Table 1 above, the calculated mean grain size decreases with the introduction of Si. This trend reflects the grain growth inhibition by the amorphous Si N_x nano-layer [8,57,58].

3.4. Chemical Composition

Figure 6 presents the EPMA-detected global composition of (AlTiZrHfTa) N_x /Si N_x RHECs deposited at $R_{N_2} = 10\%$. The increase in silicon percentage in RHECs along with the increase in I_{Si} suggest that the newly added element may be effectively incorporated into the nitride layer as expected.

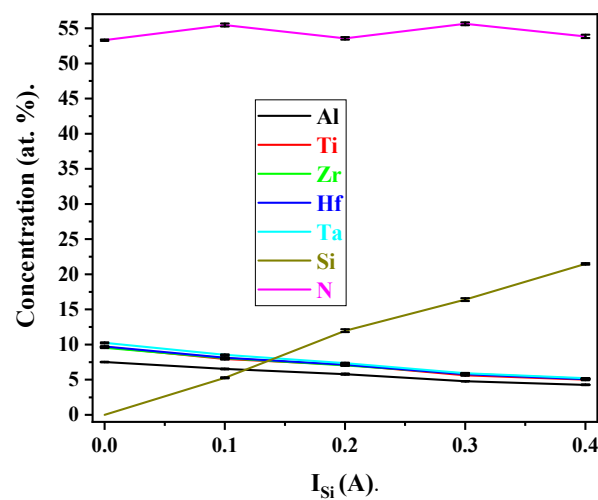


Figure 6. EPMA average element contents for FCC (AlTiZrHfTa) N_x /a-Si N_x coatings deposited at $R_{N_2} = 10\%$ as a function of I_{Si} .

The chemical composition of the (AlTiZrHfTa) N_x coating is as follows: Al = 7.5 at.%, Ti = 9.7 at.%, Zr = 9.5 at.%, Hf = 9.7 at.%, Ta = 10.3 at.%, and N = 53.3 at.%. The amount of Al was shown to be low in comparison to the target content (20 at.%). This phenomenon was explained in reference [42]. The composition stabilization of N content in the high-entropy nitride at $R_{N_2} = 10\%$ is associated with the stabilization of the crystalline nitride solid solution and target poisoning [62].

As I_{Si} increased from 0.1 A to 0.4 A, the atomic percentage of Si in the FCC(AlTiZrHfTa) N_x /a-Si N_x deposited coatings raises from 5.3 at.% to 21.5 at.%, respectively (Table 2). Moreover, the contents of metals slightly decrease, resulting from the increase in silicon percentage and the formation of nitride structure.

Table 2. Applied current on Si target I_{Si} (A) and associated global Si percentage (at.%) into the FCC (AlTiZrHfTa)-N/a-Si N_x coatings.

I_{Si} (A)	Corresponding Si Atomic Percentage (at.%)
0	0
0.1	5.3
0.2	12
0.3	16.4
0.4	21.5

3.5. Mechanical Properties

Hardness and Young's Modulus of FCC(AlTiZrHfTa) N_x /a-Si N_x Thin Coatings

Figure 7 depicts the evolution of hardness (H) and Young's modulus (E) of FCC (AlTiZrHfTa) N_x /a-Si N_x ($R_{N_2} = 10\%$) coatings as a function of I_{Si} . H decreased from 24.4 ± 0.3 GPa to 17.7 ± 0.5 GPa, while the Young's modulus also decreased from 189.0 ± 1.7 GPa to around 162.5 ± 1.6 GPa. This is due to the formation of a nano-layered architecture (amorphous Si N_x nano-layers and FCC crystalline (AlTiZrHfTa) N_x nano-layers). The amorphous nano-layer (Si N_x) hinders the growth of (AlTiZrHfTa) N_x crystallites, leading to a sudden orientation drop as revealed in XRD patterns (cf. Figure 4) [63].

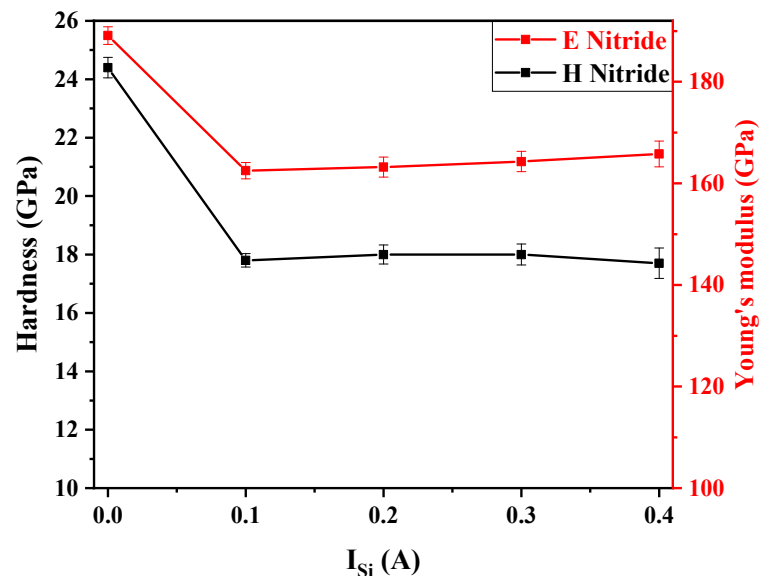


Figure 7. Hardness and Young's modulus of (AlTiZrHfTa) N_x /a-Si N_x , $R_{N_2} = 10\%$, coatings at various I_{Si} (A).

In general, nano-layered architecture leads to the hardness enhancement of the coating due to the blocking of dislocation movements at interfaces [57]. For example TiN/Si $_3$ N $_4$ multilayers exhibited a hardness enhancement with Si $_3$ N $_4$ layer thickness less than 1 nm (about 0.5 or 0.7 nm) [64,65]. However, Dong et al. [66] reported a change in hardness trend as a function of Si $_3$ N $_4$ layer thickness for ZrN/Si $_3$ N $_4$ nano-layered coating. Indeed, when the Si $_3$ N $_4$ layer thickness is about 0.6 nm, the hardness is increased, due to the formation of a crystallized Si $_3$ N $_4$ nano-layer forming coherent interfaces with the ZrN layer. However, when the thickness exceeds 1.1 nm, an amorphous growth of Si $_3$ N $_4$ is observed, resulting in a significant hardness decrease. In our study we can consider that the non-isostructural nano-layered coating associated with the amorphous Si N_x with a thickness of 1.5 nm leads to a decline of mechanical properties. Similar trends have been observed for nano-layered coatings like Cr $_2$ N/Si $_3$ N $_4$ [67], HfN/Si $_3$ N $_4$ [68], and NbN/Si $_3$ N $_4$ [69].

3.6. High-Temperature Oxidation Property

3.6.1. Oxidation Resistance of FCC(AlTiZrHfTa) N_x /a-Si N_x Coatings

Figure 8 depicts the dynamic thermogravimetric analysis (TGA) curves of the FCC (AlTiZrHfTa) N_x and FCC (AlTiZrHfTa) N_x /a-Si N_x coatings from room temperature (RT) to 800 °C. The weight gain of the FCC (AlTiZrHfTa) N_x coating (Figure 8) grows steadily between RT and 694 °C, followed by a rapid growth at higher temperatures. When the FCC (AlTiZrHfTa) N_x /a-Si N_x RHECs are deposited, the weight gain shows a drastic growth only after around 703 °C (for the RHECs obtained for $I_{Si} = 0.1$ A) but is largely lower than that of the FCC (AlTiZrHfTa) N_x coating. When the Si content increases further, the critical oxidation temperature exceeds 800 °C.

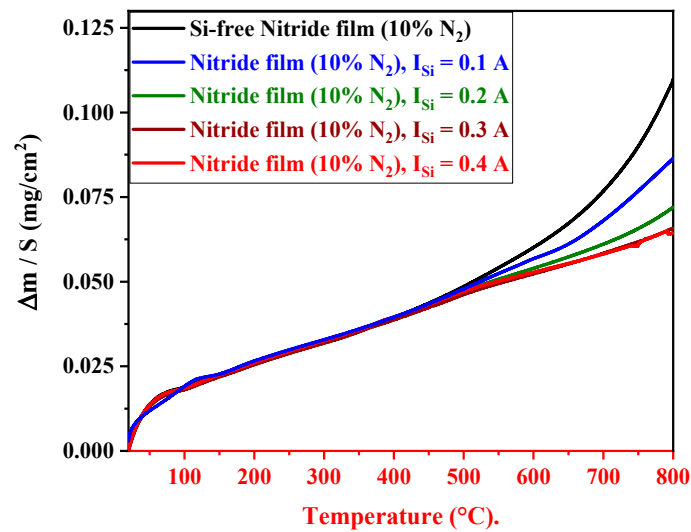


Figure 8. Weight gain per unit surface area ($\frac{\Delta m}{S}$, $\frac{\text{mg}}{\text{cm}^2}$) as a function of temperature ($^{\circ}\text{C}$) for FCC (AlTiZrHfTa)N and FCC (AlTiZrHfTa) N_x /a-Si N_x RHECs at $R_{N_2} = 10\%$ obtained for various I_{Si} .

3.6.2. Oxidation Kinetics of FCC(AlTiZrHfTa) N_x /a-Si N_x Coatings

Figure 9 illustrates the isothermal thermogravimetric curves plotted during 1 h of exposure at 800 $^{\circ}\text{C}$ for FCC (AlTiZrHfTa) N_x /a-Si N_x coatings obtained for various I_{Si} .

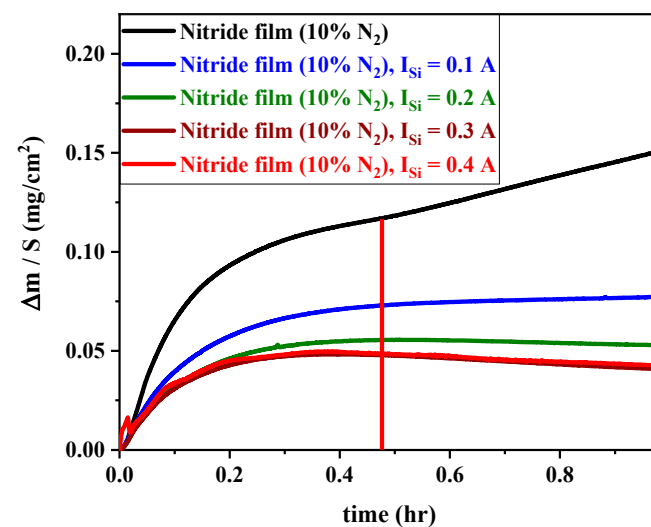


Figure 9. Oxidation kinetic curves FCC (AlTiZrHfTa) N_x /a-Si N_x coatings at $R_{N_2} = 10\%$ obtained for various I_{Si} at 800 $^{\circ}\text{C}$ (The vertical red line delimits the ending of parabolic growth and the beginning of the linear growth for the nitride film, black curve).

In the case of (AlTiZrHfTa) N_x nitride coatings, there is an initial slower parabolic weight gain growth up to 0.112 mg/cm^2 , followed by a quick linear increase after around 28 min of oxidation. The linear rate law following by the parabolic growth (Figure 9) is related to breakaway oxidation effect. The linear weight gain is assumed to represent a change in the scale structure by formation of thick, porous oxide scale promoting a significant access of gaseous species towards the coating phase [70]. Gorr et al. [71] noticed a similar variation for the NbMoCrTiAl-1Si arc melted HEA.

When FCC (AlTiZrHfTa) N_x /a-Si N_x is deposited, the weight gain is drastically decreased. In addition, the breakaway point completely disappeared, which could be explained by the protectiveness enhancement of the new formed oxide [70,72].

Structure Analysis of Oxidized FCC(AlTiZrHfTa) N_x /a-Si N_x Coatings

Figure 10 presents the XRD patterns of (AlTiZrHfTa) N_x /a-Si N_x RHECs before and after 1 h of isothermal oxidation at 800 °C in a dry-air atmosphere. After oxidation, we noted a presence of a peak at $2\theta \approx 30^\circ$, which could be identified as zirconia (ZrO $_2$). In addition, a broadening of (111) and (222) peaks occur after oxidation. This broadening could be attributed to the formation of oxides [55,73]. For the (AlTiZrHfTa) N_x /a-Si N_x RHECs, no significant changes have been observed on XRD patterns whatever the current intensity on the Si target. At this stage, this analysis is not able to identify the oxide nature (complementary TEM and SEM results are presented below). It should be noted that neither peeling nor coating removal was observed on the annealed samples.

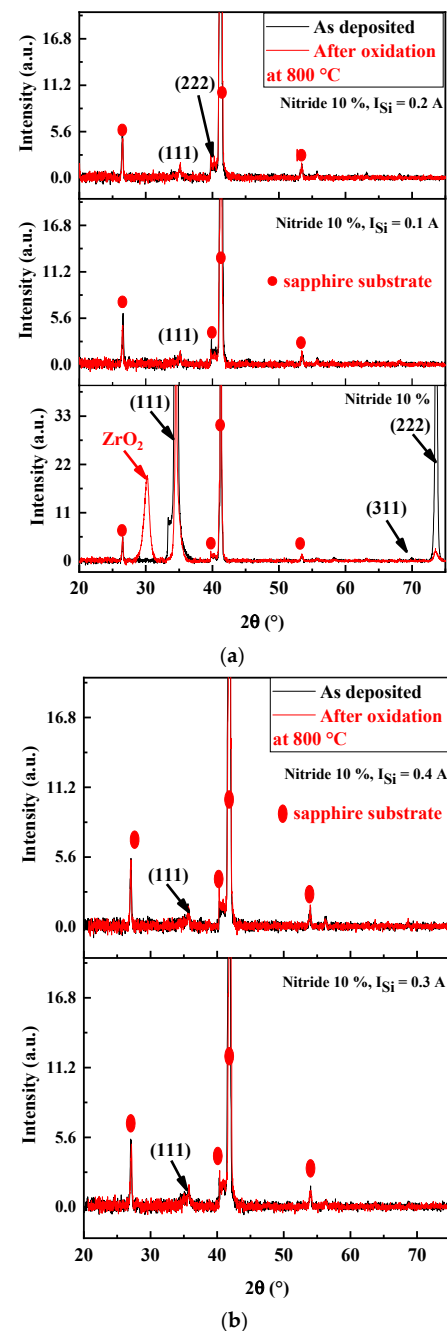


Figure 10. X-ray diffraction patterns of (a) (AlTiZrHfTa) N_x nitride coatings and FCC (AlTiZrHfTa) N_x /a-Si N_x coatings obtained for $I = 0.1$ and 0.2 A. (b) FCC (AlTiZrHfTa) N_x /a-Si N_x coatings obtained for $I = 0.3$ and 0.4 A before and after 1 h of oxidation at 800 °C in a dry-air atmosphere.

Morphology Analysis of Oxidized FCC(AlTiZrHfTa) N_x /a-Si N_x Coatings

To better understand of the evolution of the morphology of (AlTiZrHfTa) N_x /a-Si N_x RHECs following the oxidation process, SEM was used to investigate (AlTiZrHfTa) N_x and FCC (AlTiZrHfTa) N_x /a-Si N_x obtained for $I_{Si} = 0.2$ A. Figure 11 shows their surface and cross-sectional morphologies, after 1 h of isothermal oxidation at 800 °C in a dry-air atmosphere. Figure 11f,h clearly illustrates the presence of cracks and pores on the coating's surfaces. In the case of the FCC (AlTiZrHfTa) N_x /a-Si N_x coatings, obtained for $I_{Si} = 0.2$ A, the oxide layer is thinner, which indicates a better oxidation resistance compared to (AlTiZrHfTa) N_x coatings (cf. Figure 9).

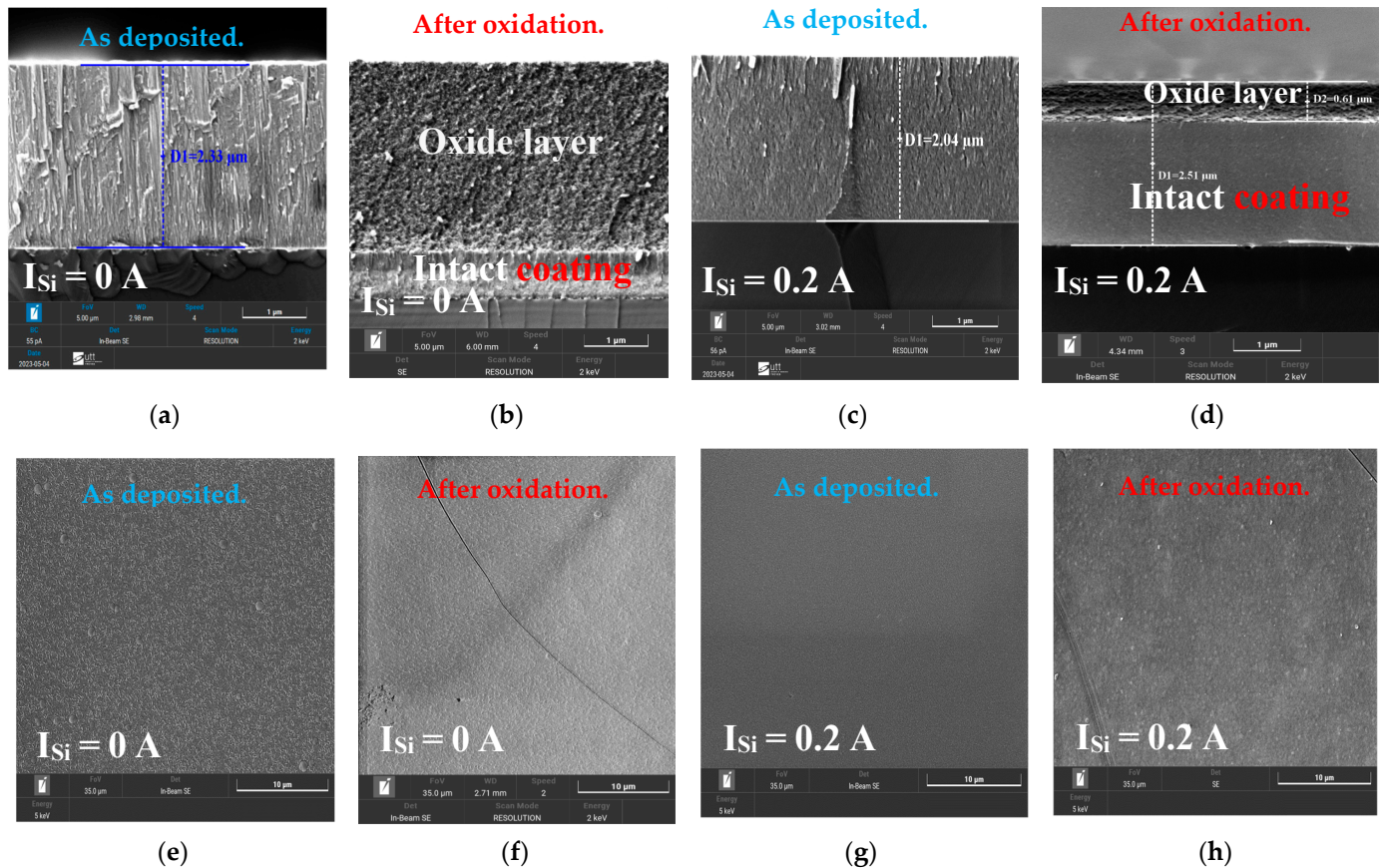


Figure 11. Cross-sectional and surface SEM micrographs of (AlTiZrHfTa) N_x (AlTiZrHfTa) N_x RHECs (a,e) as deposited and (b,f) after 1 h oxidation at 800 °C, and FCC (AlTiZrHfTa) N_x /a-Si N_x RHECs obtained for $I_{Si} = 0.2$ A (c,g) as deposited and (d,h) after 1 h oxidation at 800 °C.

Microstructure Investigation of Oxidized FCC(AlTiZrHfTa) N_x /a-Si N_x RHECs

The cross-sectional microstructure of oxidized (AlTiZrHfTa) N_x RHECs at $R_{N_2} = 10\%$ and the (AlTiZrHfTa) N_x /a-Si N_x coating obtained for $I_{Si} = 0.2$ A was analyzed by using TEM (Figure 12). The as-deposited (AlTiZrHfTa) N_x nitride coating exhibits a columnar growth (Figure 12a) with (111) preferred orientation as shown by the inset SAED pattern. After oxidation, the (AlTiZrHfTa) N_x nitride coating reveals two separate zones: an intact coating with black contrast at the bottom and a homogeneous thick (≈ 2.5 μm , Figure 11b) and porous oxide layer on the top (depicted in reference [42]). For FCC (AlTiZrHfTa) N_x /a-Si N_x coating, obtained for $I_{Si} = 0.2$ A, a nano-layered architecture is observed (cf. Figure 2b). After oxidation of the (AlTiZrHfTa) N_x /Si N_x coating, two different zones are observed as well: intact coating with a nano-layered architecture at the bottom (Figure 12e) and a homogeneous thin (≈ 600 nm) and porous oxide layer on the top (Figure 12d,e).

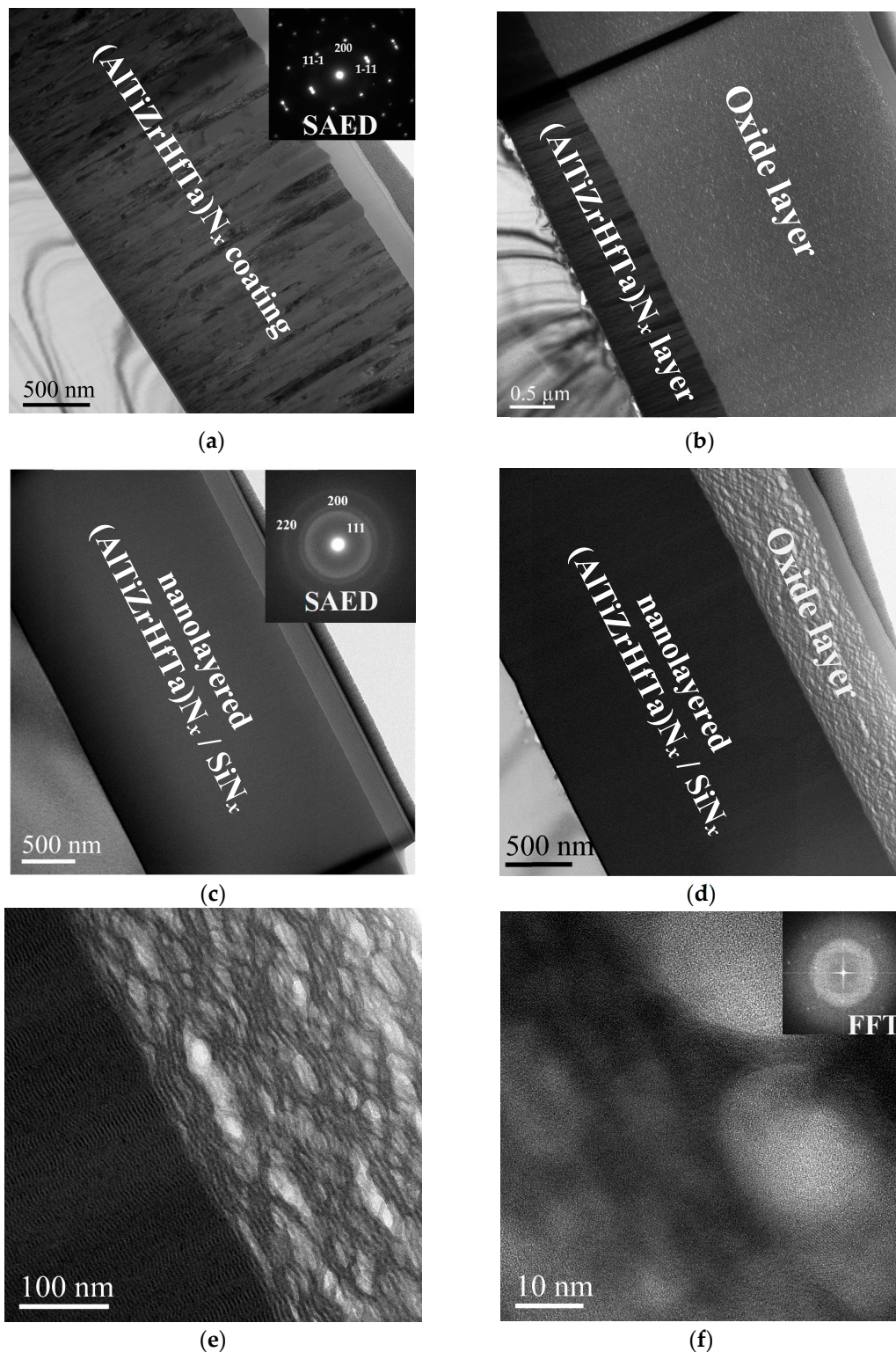


Figure 12. (a) Bright field TEM micrograph of intact nitride coating obtained with $R_{N_2} = 10\%$ with associated SAED pattern. (b) Bright field TEM micrograph of the same coating after 1 h of oxidation at 800 °C. (c) Bright field TEM micrograph of intact FCC $(AlTiZrHfTa)_x/a-Si_3N_x$ coating obtained for $I_{Si} = 0.2$ A with associated SAED pattern. (d) Bright field TEM micrograph of the FCC $(AlTiZrHfTa)_x/a-Si_3N_x$ coating obtained for $I_{Si} = 0.2$ A after 1 h of oxidation at 800 °C. (e) Zoom-in on oxidized layer of FCC $(AlTiZrHfTa)_x/a-Si_3N_x$ coating obtained for $I_{Si} = 0.2$ A coating. (f) HRTEM and associated FFT of oxidized zone of FCC $(AlTiZrHfTa)_x/a-Si_3N_x$ coating obtained for $I_{Si} = 0.2$ A.

HRTEM image of the oxide of the $(\text{AlTiZrHfTa})\text{N}_x/\text{SiN}_x$ coating, obtained for $I_{\text{Si}} = 0.2 \text{ A}$, is presented in Figure 12f. The oxide layer exhibits an amorphous aspect. This is further verified by the corresponding FFT pattern, which shows a circular diffuse ring (Figure 11f).

STEM-EDS mapping of the FCC $(\text{AlTiZrHfTa})\text{N}_x/a\text{-SiN}_x$ coating obtained for $I_{\text{Si}} = 0.2 \text{ A}$, before and after the oxidation process on the oxidized zone area, was performed. The results are presented in the (Figure 13).

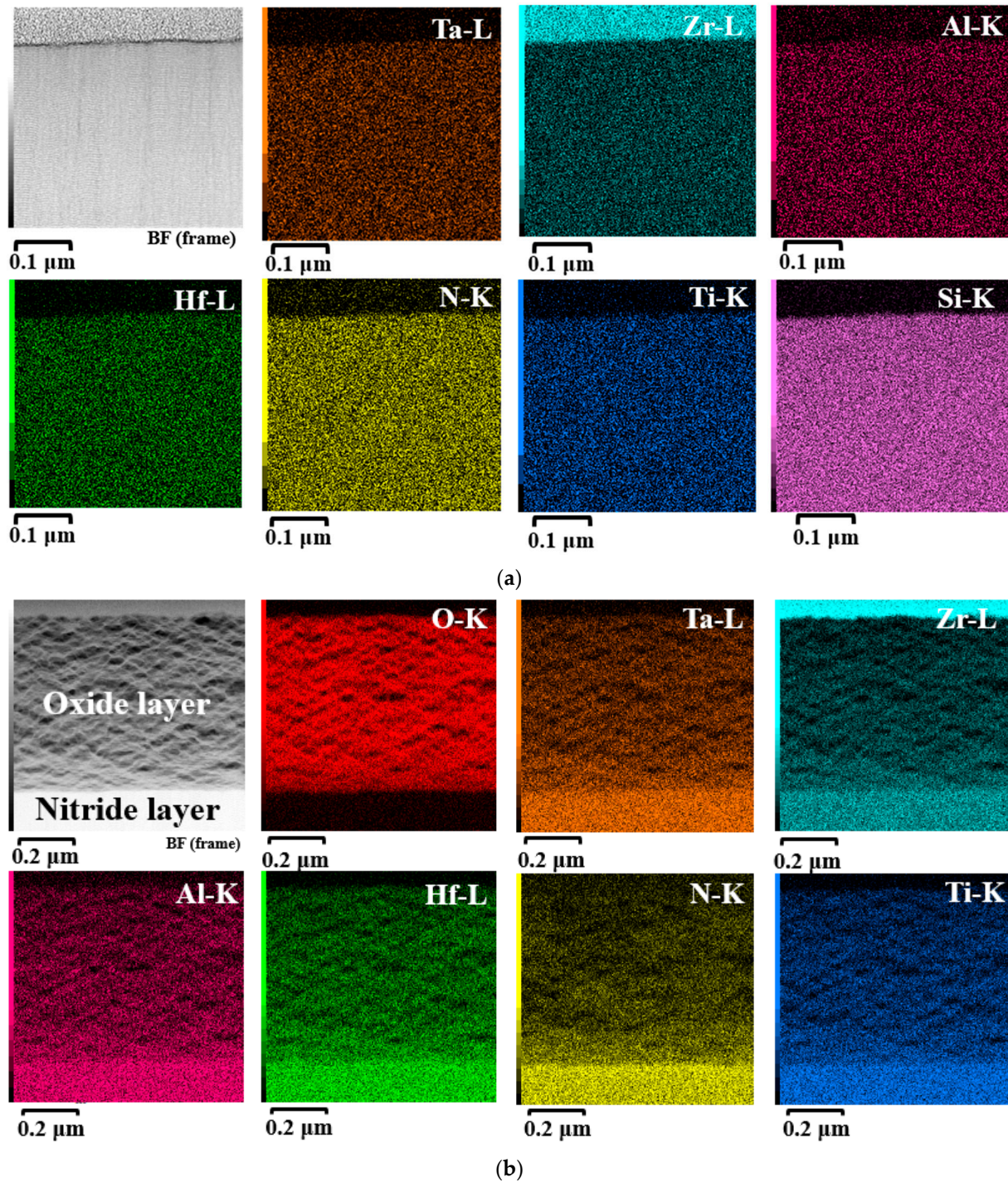


Figure 13. STEM EDS mapping of the FCC $(\text{AlTiZrHfTa})\text{N}_x/a\text{-SiN}_x$ coating obtained for $I_{\text{Si}} = 0.2 \text{ A}$: (a) sections before and (b) zoom-in on oxidized zone after 1 h of oxidation at $800 \text{ }^\circ\text{C}$.

After 1 h of oxidation at 800 °C, we found a uniform distribution of metallic elements throughout the (AlTiZrHfTa) N_x /Si N_x RHECs and oxide layer (Figure 13). As a result, a mixed oxide is formed [74]. It should be noted that the amorphous aspect of the oxide layer has also been observed for the (AlTiZrHfTa) N_x nitride coating [42].

Oxidation Rate through k_p Analysis

Figure 14 traces the parabolic rate constant k_p $g^2 cm^{-4} h^{-1}$ at 800 °C for the investigated (AlTiZrHfTa) N_x and (AlTiZrHfTa) N_x /Si N_x coatings. k_p is calculated according to (Equation (1)) [75]. For the (AlTiZrHfTa) N_x coating, k_p is calculated at $3.36 \times 10^{-8} g^2 cm^{-4} h^{-1}$ for the sample tested at 800 °C. However, in the case of the (AlTiZrHfTa) N_x /Si N_x coating, obtained for $I_{Si} = 0.2$ A, the kinetic constant k_p decreased to $6.06 \times 10^{-9} g^2 cm^{-4} h^{-1}$ (Figure 14). This decreasing tendency sustains the previous oxidation kinetic curves' evolution (cf. Figure 9), revealing an oxidation resistance enhancement of the (AlTiZrHfTa) N_x /Si N_x coating compared to the (AlTiZrHfTa) N_x coating.

$$\left(\frac{\Delta m}{S}\right)^2 = k_p \cdot t, \quad (1)$$

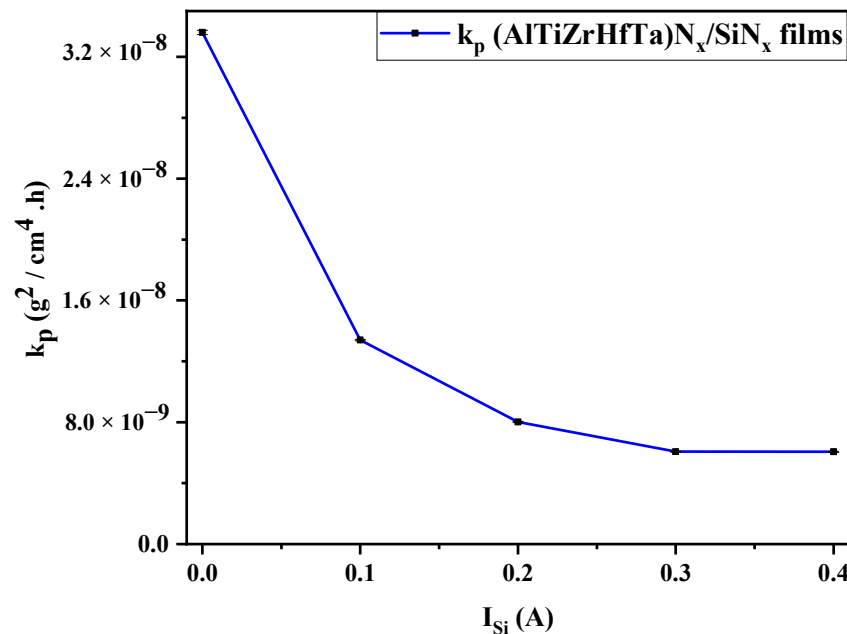


Figure 14. Kinetic constant k_p of FCC (AlTiZrHfTa) N_x /a-Si N_x nitride coatings obtained at ($R_{N_2} = 10\%$) after 1 h of oxidation at 800 °C as a function of I_{Si} (A).

Activation Energy E_a

The oxidation activation energy (E_a) is of fundamental importance to understanding the oxidation mechanisms. It can be evaluated from the Arrhenius formula (Equation (2)) [76], by linear fitting of the kinetic constant (oxidation rate) at different oxidation temperatures (700 °C, 750 °C, and 800 °C):

$$k_p = k_{p0} \exp\left(-\frac{E_a}{R T}\right), \quad (2)$$

R: molar gas constant, k_{p0} : oxidation rate constant, and T: temperature.

The activation energy of (AlTiZrHfTa) N_x nitride coating was equal to 90.8 $kJ \cdot mol^{-1}$ [42]. However, the activation energy increases to a value of 126.52 $kJ \cdot mol^{-1}$ for the (AlTiZrHfTa) N_x /Si N_x coating obtained for $I_{Si} = 0.2$ A (Table 3). Even at this oxidation enhancement, the values remain low when compared to those of other alloys, as shown in Table 3.

Table 3. Activation energy E_a of Si-free nitride coating and Si-doped (AlTiZrHfTa) N_x /a-Si N_x coating obtained for $I_{Si} = 0.2$ A, and different investigated thin coatings [42,77,78].

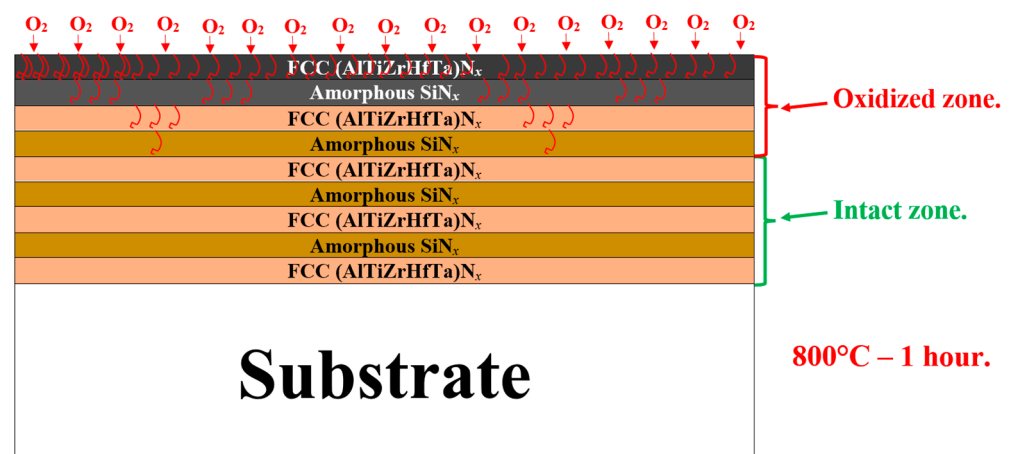
Coating	E_a (Activation Energy) (kJ·mol ⁻¹)	E_a Error	Reference
(AlTiZrHfTa) N_x ($R_{N_2} = 10\%$)	90.8	0.05	[42]
(AlTiZrHfTa) N_x /Si N_x ($R_{N_2} = 10\%$, $I_{Si} = 0.2$ A)	126.52	0.02	This study
CrN	243	-	[77]
CrAlN	280	-	[77]
TiN	193	-	[77]
TiSiN	260	-	[77]
(AlCrTaTiZr) N	208.6	-	[78]

3.6.3. Discussion of the Oxidation Mechanisms

The present study explored the oxidation resistance of FCC (AlTiZrHfTa) N_x /Si N_x thin coatings. When Si is introduced, the oxidation resistance is drastically enhanced, according to various parameters such as the increase in oxidation temperature, breakaway disappearance, on weight gain curve, and k_p decreasing trend during 1 h of oxidation at 800 °C (cf. Figures 8, 9 and 14). SEM and TEM analyses illustrated the formation of a dense nano-layered architecture due to the sweeping mode during the deposition process. Moreover, XPS and XRD patterns depicted the presence of FCC (AlTiZrHfTa) N_x and amorphous Si N_x phases.

It should be mentioned that the amorphous (Si N_x) layer is known for its elevated resistance to oxygen diffusion at high temperatures [56,66,79,80]. Moreover, the oxidation rate decrease could also be related to a relatively smaller residual stress throughout the coating, as a result of multiple interfaces between the formed nano-layers [36,81–83]. This phenomenon differs significantly from monolithically grown (AlTiZrHfTa) N_x 's oxidation behavior (Figures 9 and 11). In addition, the high number of interfaces of FCC (AlTiZrHfTa)N/a-Si N_x nano-layers lead to a reduction in the interconnection of pores and defects penetrating through the coating that may result in oxygen diffusion into the oxidized coating [83].

A schematic model is proposed in Figure 15 to illustrate the Si N_x inhibiting effect, when the (AlTiZrHfTa) N_x /a-Si N_x thin coating is exposed to oxygen. Because of their amorphous nature, Si N_x nano-layers act as barrier layers (shields), which could inhibit the mutual diffusion of additional metallic atoms and decreases the oxidation reaction [36]. Steyer et.al [84] showed the oxidation resistance enhancement of TiN coating by the segregation of amorphous Si N_x at the grain boundaries, leading to an increase in the protective shielding effect. The results reported in this study verified that a coating synthesized by the current alloy design efficiently slowed the oxidation rate.

**Figure 15.** Schematic drawing, illustrating the oxidation behavior of the nitride coatings in the presence of Si.

4. Conclusions

(AlTiZrHfTa) N_x /Si N_x RHECs were synthesized by DCMS in two nitrogen ratios ($R_{N_2} = 0\%$ and 10%).

The effect of Si's addition on the structure, microstructure, mechanical properties, and oxidation behavior were investigated. The current study is mainly focused on the oxidation resistance enhancement of these so-called "refractory" HEA coatings by using an alloying approach and promoting nano-layered architecture.

- The deposition of nano-layered FCC (AlTiZrHfTa) N_x /a-Si N_x coatings results in a density increase in the nitride coatings.
- The deposition of the nano-layered FCC (AlTiZrHfTa) N_x /a-Si N_x coatings leads to the decrease in hardness and Young's modulus up to $H = 17.7 \pm 0.5$ GPa and $E = 162.5 \pm 1.6$ GPa. The softening of the coatings results from the formation of the amorphous Si N_x nano-layers, hindering the growth of the FCC (AlTiZrHfTa) N_x nano-layers.
- The deposition of the nano-layered FCC (AlTiZrHfTa) N_x /a-Si N_x coating improved the oxidation resistance at 800°C . The increase in I_{Si} significantly decreased the parabolic rate constant k_p from $3.36 \times 10^{-8} \text{ g}^2 \text{ cm}^{-4} \text{ h}^{-1}$ for FCC (AlTiZrHfTa) N_x coating to $6.06 \times 10^{-9} \text{ g}^2 \text{ cm}^{-4} \text{ h}^{-1}$ for FCC (AlTiZrHfTa) N_x /a-Si N_x coatings at 800°C .
- The activation energy E_a has increased from $90.8 \text{ kJ}\cdot\text{mol}^{-1}$ for the FCC (AlTiZrHfTa) N_x coating to $126.52 \text{ kJ}\cdot\text{mol}^{-1}$ for the FCC (AlTiZrHfTa) N_x /a-Si N_x coating obtained for $I_{Si} = 0.2$ A. This trend reflects an oxidation resistance improvement due to the formation of the amorphous Si N_x nano-layer in alternance with FCC (AlTiZrHfTa) N_x .

The deposition of FCC (AlTiZrHfTa) N_x /a-Si N_x results in the formation of an inhibiting amorphous Si N_x nano-layer, protecting FCC (AlTiZrHfTa) N_x crystallites from oxygen onslaught, thus improving their oxidation resistance.

The results obtained in this study illustrate the effectiveness of using an alloying approach to further enhance the RHEAs' efficiency, particularly toward high-temperature applications.

Author Contributions: Conceptualization, D.E.T., F.S. (Frederic Sanchette) and M.E.G.; methodology, D.E.T., S.A., F.S. (Frederic Sanchette) and M.E.G.; validation, D.E.T., S.A., F.S. (Frederic Sanchette) and M.E.G.; formal analysis, D.E.T., A.B., J.G. and A.G.; investigation, D.E.T., A.B., J.G., A.G., P.S.P. and M.M.C.; resources, F.P.; data curation, D.E.T., P.S.P., M.M.C. and M.E.G.; writing—original draft preparation, D.E.T.; writing—review and editing, D.E.T., S.A., A.B., F.S. (Frederic Sanchette) and M.E.G.; visualization, D.E.T., F.P., F.S. (Frederic Schuster), F.S. (Frederic Sanchette) and M.E.G.; supervision, F.S. (Frederic Sanchette) and M.E.G.; project administration, F.S. (Frederic Schuster); funding acquisition, F.S. (Frederic Schuster) and F.S. (Frederic Sanchette). All authors have read and agreed to the published version of the manuscript.

Funding: This research was funded by Le Groupement d'Intérêt Public Haute-Marne—GIP52 (no number), and La Direction du programme Transversal de compétences Matériaux et Procédés de Commissariat à l'Énergie Atomique et aux énergies alternatives (CEA) (no number).

Institutional Review Board Statement: Not applicable.

Informed Consent Statement: Not applicable.

Data Availability Statement: The raw data supporting the conclusions of this article will be made available by the authors on request.

Acknowledgments: The authors thank the Université de Technologie de Troyes (UTT) and the central laboratories of TPU (Analytical Center) for the XPS measurements.

Conflicts of Interest: The authors declare no conflicts of interest.

References

1. Holleck, H. Material Selection for Hard Coatings. *J. Vac. Sci. Technol. A* **1986**, *4*, 2661–2669. [[CrossRef](#)]
2. Sundgren, J.-E.; Hentzell, H.T.G. A Review of the Present State of Art in Hard Coatings Grown from the Vapor Phase. *J. Vac. Sci. Technol. A* **1986**, *4*, 2259–2279. [[CrossRef](#)]

3. Panjan, P.; Navinšek, B.; Cvelbar, A.; Zalar, A.; Milošev, I. Oxidation of TiN, ZrN, TiZrN, CrN, TiCrN and TiN/CrN Multilayer Hard Coatings Reactively Sputtered at Low Temperature. *Thin Solid Film.* **1996**, *281–282*, 298–301. [[CrossRef](#)]
4. Barshilia, H.C.; Selvakumar, N.; Deepthi, B.; Rajam, K.S. A Comparative Study of Reactive Direct Current Magnetron Sputtered CrAlN and CrN Coatings. *Surf. Coat. Technol.* **2006**, *201*, 2193–2201. [[CrossRef](#)]
5. Uchida, M.; Nihira, N.; Mitsuo, A.; Toyoda, K.; Kubota, K.; Aizawa, T. Friction and Wear Properties of CrAlN and CrVN Films Deposited by Cathodic Arc Ion Plating Method. *Surf. Coat. Technol.* **2004**, *177–178*, 627–630. [[CrossRef](#)]
6. Zhang, H.; Zou, Y.; Zou, Z.; Wu, D. Microstructures and Properties of Low-Chromium High Corrosion-Resistant TiC–VC Reinforced Fe-Based Laser Cladding Layer. *J. Alloys Compd.* **2015**, *622*, 62–68. [[CrossRef](#)]
7. Choi, P.-P.; Povstugar, I.; Ahn, J.-P.; Kostka, A.; Raabe, D. Thermal Stability of TiAlN/CrN Multilayer Coatings Studied by Atom Probe Tomography. *Ultramicroscopy* **2011**, *111*, 518–523. [[CrossRef](#)] [[PubMed](#)]
8. Barshilia, H.C.; Deepthi, B.; Arun Prabhu, A.S.; Rajam, K.S. Superhard Nanocomposite Coatings of TiN/Si₃N₄ Prepared by Reactive Direct Current Unbalanced Magnetron Sputtering. *Surf. Coat. Technol.* **2006**, *201*, 329–337. [[CrossRef](#)]
9. Li, C.; Wang, L.; Shang, L.; Cao, X.; Zhang, G.; Yu, Y.; Li, W.; Zhang, S.; Hu, H. Mechanical and High-Temperature Tribological Properties of CrAlN/TiSiN Multilayer Coating Deposited by PVD. *Ceram. Int.* **2021**, *47*, 29285–29294. [[CrossRef](#)]
10. Fu, T.; Zhang, Z.; Peng, X.; Weng, S.; Miao, Y.; Zhao, Y.; Fu, S.; Hu, N. Effects of Modulation Periods on Mechanical Properties of V/VN Nano-Multilayers. *Ceram. Int.* **2019**, *45*, 10295–10303. [[CrossRef](#)]
11. Çomaklı, O. Influence of CrN, TiAlN Monolayers and TiAlN/CrN Multilayer Ceramic Films on Structural, Mechanical and Tribological Behavior of β -Type Ti45Nb Alloys. *Ceram. Int.* **2020**, *46*, 8185–8191. [[CrossRef](#)]
12. Chang, Y.-Y.; Yang, Y.-J.; Weng, S.-Y. Effect of Interlayer Design on the Mechanical Properties of AlTiCrN and Multilayered AlTiCrN/TiSiN Hard Coatings. *Surf. Coat. Technol.* **2020**, *389*, 125637. [[CrossRef](#)]
13. Chan, Y.-C.; Chen, H.-W.; Chao, P.-S.; Duh, J.-G.; Lee, J.-W. Microstructure Control in TiAlN/Si_xN_y Multilayers with Appropriate Thickness Ratios for Improvement of Hardness and Anti-Corrosion Characteristics. *Vacuum* **2013**, *87*, 195–199. [[CrossRef](#)]
14. Chen, S.N.; Zhao, Y.M.; Zhang, Y.F.; Chen, L.; Liao, B.; Zhang, X.; Ouyang, X.P. Influence of Carbon Content on the Structure and Tribocorrosion Properties of TiAlCN/TiAlN/TiAl Multilayer Composite Coatings. *Surf. Coat. Technol.* **2021**, *411*, 126886. [[CrossRef](#)]
15. Yue, J.; Li, G. Microstructure and Mechanical Properties of TiAlN/Si₃N₄ Nano-Multilayers Synthesized by Reactive Magnetron Sputtering. *J. Alloys Compd.* **2009**, *481*, 710–713. [[CrossRef](#)]
16. Vepřek, S.; Reiprich, S. A Concept for the Design of Novel Superhard Coatings. *Thin Solid Film.* **1995**, *268*, 64–71. [[CrossRef](#)]
17. Yeh, J.-W. Alloy Design Strategies and Future Trends in High-Entropy Alloys. *JOM* **2013**, *65*, 1759–1771. [[CrossRef](#)]
18. Tsai, M.-H.; Yeh, J.-W. High-Entropy Alloys: A Critical Review. *Mater. Res. Lett.* **2014**, *2*, 107–123. [[CrossRef](#)]
19. Ye, Y.F.; Wang, Q.; Lu, J.; Liu, C.T.; Yang, Y. High-Entropy Alloy: Challenges and Prospects. *Mater. Today* **2016**, *19*, 349–362. [[CrossRef](#)]
20. Guo, S. Phase Selection Rules for Cast High Entropy Alloys: An Overview. *Mater. Sci. Technol.* **2015**, *31*, 1223–1230. [[CrossRef](#)]
21. Guo, S.; Liu, C.T. Phase Stability in High Entropy Alloys: Formation of Solid-Solution Phase or Amorphous Phase. *Prog. Nat. Sci. Mater. Int.* **2011**, *21*, 433–446. [[CrossRef](#)]
22. Yeh, J.-W.; Lin, S.-J. Breakthrough Applications of High-Entropy Materials. *J. Mater. Res.* **2018**, *33*, 3129–3137. [[CrossRef](#)]
23. Pickering, E.J.; Carruthers, A.W.; Barron, P.J.; Middleburgh, S.C.; Armstrong, D.E.J.; Gandy, A.S. High-Entropy Alloys for Advanced Nuclear Applications. *Entropy* **2021**, *23*, 98. [[CrossRef](#)] [[PubMed](#)]
24. Yu, W.; Li, W.; Liu, P.; Zhang, K.; Ma, F.; Chen, X.; Feng, R.; Liaw, P.K. Silicon-Content-Dependent Microstructures and Mechanical Behavior of (AlCrTiZrMo)-Six-N High-Entropy Alloy Nitride Films. *Mater. Des.* **2021**, *203*, 109553. [[CrossRef](#)]
25. Chang, S.-Y.; Li, C.-E.; Chiang, S.-C.; Huang, Y.-C. 4-Nm Thick Multilayer Structure of Multi-Component (AlCrRuTaTiZr)_{N_x} as Robust Diffusion Barrier for Cu Interconnects. *J. Alloys Compd.* **2012**, *515*, 4–7. [[CrossRef](#)]
26. Milošev, I.; Strehblow, H.-H.; Navinšek, B. Comparison of TiN, ZrN and CrN Hard Nitride Coatings: Electrochemical and Thermal Oxidation. *Thin Solid Film.* **1997**, *303*, 246–254. [[CrossRef](#)]
27. Kehal, A.; Saoula, N.; Abaidia, S.-E.-H.; Nouveau, C. Effect of Ar/N₂ Flow Ratio on the Microstructure and Mechanical Properties of Ti-Cr-N Coatings Deposited by DC Magnetron Sputtering on AISI D2 Tool Steels. *Surf. Coat. Technol.* **2021**, *421*, 127444. [[CrossRef](#)]
28. Senkov, O.N.; Miracle, D.B.; Chaput, K.J.; Couzinie, J.-P. Development and Exploration of Refractory High Entropy Alloys—A Review. *J. Mater. Res.* **2018**, *33*, 3092–3128. [[CrossRef](#)]
29. Sheikh, S.; Gan, L.; Tsao, T.-K.; Murakami, H.; Shafeie, S.; Guo, S. Aluminizing for Enhanced Oxidation Resistance of Ductile Refractory High-Entropy Alloys. *Intermetallics* **2018**, *103*, 40–51. [[CrossRef](#)]
30. El Garah, M.; Soubane, D.; Sanchette, F. Review on Mechanical and Functional Properties of Refractory High-Entropy Alloy Films by Magnetron Sputtering. *Emergent Mater.* **2023**, *7*, 77–101. [[CrossRef](#)]
31. DiStefano, J.R.; Hendricks, J.W. Oxidation Rates of Niobium and Tantalum Alloys at Low Pressures. *Oxid. Met.* **1994**, *41*, 365–376. [[CrossRef](#)]
32. Zelenitsas, K.; Tsakiroopoulos, P. Effect of Al, Cr and Ta Additions on the Oxidation Behaviour of Nb–Ti–Si in Situ Composites at 800 °C. *Mater. Sci. Eng. A* **2006**, *416*, 269–280. [[CrossRef](#)]
33. Kim, B.G.; Kim, G.M.; Kim, C.J. Oxidation Behavior of TiAl-X (X = Cr, V, Si, Mo or Nb) Intermetallics at Elevated Temperature. *Scr. Metall. Mater.* **1995**, *33*, 1117–1125. [[CrossRef](#)]

34. Moricca, M.D.P.; Varma, S.K. High Temperature Oxidation Characteristics of Nb–10W–XCr Alloys. *J. Alloys Compd.* **2010**, *489*, 195–201. [[CrossRef](#)]
35. Müller, F.; Gorr, B.; Christ, H.-J.; Müller, J.; Butz, B.; Chen, H.; Kauffmann, A.; Heilmaier, M. On the Oxidation Mechanism of Refractory High Entropy Alloys. *Corros. Sci.* **2019**, *159*, 108161. [[CrossRef](#)]
36. Tsai, D.-C.; Deng, M.-J.; Chang, Z.-C.; Kuo, B.-H.; Chen, E.-C.; Chang, S.-Y.; Shieu, F.-S. Oxidation Resistance and Characterization of (AlCrMoTaTi)-Six-N Coating Deposited via Magnetron Sputtering. *J. Alloys Compd.* **2015**, *647*, 179–188. [[CrossRef](#)]
37. Bagdasaryan, A.A.; Pshyk, A.V.; Coy, L.E.; Konarski, P.; Misnik, M.; Ivashchenko, V.I.; Kempinski, M.; Mediuikh, N.R.; Pogrebnyak, A.D.; Beresnev, V.M.; et al. A New Type of (TiZrNbTaHf)N/MoN Nanocomposite Coating: Microstructure and Properties Depending on Energy of Incident Ions. *Compos. Part B Eng.* **2018**, *146*, 132–144. [[CrossRef](#)]
38. Bagdasaryan, A.A.; Pshyk, A.V.; Coy, L.E.; Kempinski, M.; Pogrebnyak, A.D.; Beresnev, V.M.; Jurga, S. Structural and Mechanical Characterization of (TiZrNbHfTa)N/WN Multilayered Nitride Coatings. *Mater. Lett.* **2018**, *229*, 364–367. [[CrossRef](#)]
39. Zhang, W.; Tang, R.; Yang, Z.B.; Liu, C.H.; Chang, H.; Yang, J.J.; Liao, J.L.; Yang, Y.Y.; Liu, N. Preparation, Structure, and Properties of High-Entropy Alloy Multilayer Coatings for Nuclear Fuel Cladding: A Case Study of AlCrMoNbZr/(AlCrMoNbZr)N. *J. Nucl. Mater.* **2018**, *512*, 15–24. [[CrossRef](#)]
40. Zhang, W.; Wang, M.; Wang, L.; Liu, C.H.; Chang, H.; Yang, J.J.; Liao, J.L.; Yang, Y.Y.; Liu, N. Interface Stability, Mechanical and Corrosion Properties of AlCrMoNbZr/(AlCrMoNbZr)N High-Entropy Alloy Multilayer Coatings under Helium Ion Irradiation. *Appl. Surf. Sci.* **2019**, *485*, 108–118. [[CrossRef](#)]
41. Ren, B.; Zhao, R.; Zhang, G.; Liu, Z.; Cai, B.; Jiang, A. Microstructure and Properties of the AlCrMoZrTi/(AlCrMoZrTi)N Multilayer High-Entropy Nitride Ceramics Films Deposited by Reactive RF Sputtering. *Ceram. Int.* **2022**, *48*, 16901–16911. [[CrossRef](#)]
42. Touaibia, D.E.; Achache, S.; Bouissil, A.; Ghanbaja, J.; Migot, S.; Yazdi, M.A.P.; Schuster, F.; Panicaud, B.; Sanchette, F.; El Garah, M. Oxidation Resistance and Mechanical Properties of AlTiZrHfTa(-N) High Entropy Films Deposited by Reactive Magnetron Sputtering. *J. Alloys Compd.* **2023**, *969*, 172397. [[CrossRef](#)]
43. Bräuer, G.; Szyszka, B.; Vergöhl, M.; Bandorf, R. Magnetron Sputtering—Milestones of 30 Years. *Vacuum* **2010**, *84*, 1354–1359. [[CrossRef](#)]
44. Kaiser, N. Review of the Fundamentals of Thin-Film Growth. *Appl. Opt. AO* **2002**, *41*, 3053–3060. [[CrossRef](#)] [[PubMed](#)]
45. Cai, Y.P.; Wang, G.J.; Ma, Y.J.; Cao, Z.H.; Meng, X.K. High Hardness Dual-Phase High Entropy Alloy Thin Films Produced by Interface Alloying. *Scr. Mater.* **2019**, *162*, 281–285. [[CrossRef](#)]
46. Xu, Y.X.; Chen, L.; Pei, F.; Chang, K.K.; Du, Y. Effect of the Modulation Ratio on the Interface Structure of TiAlN/TiN and TiAlN/ZrN Multilayers: First-Principles and Experimental Investigations. *Acta Mater.* **2017**, *130*, 281–288. [[CrossRef](#)]
47. El Garah, M.; Touaibia, D.E.; Achache, S.; Michau, A.; Sviridova, E.; Postnikov, P.S.; Chehimi, M.M.; Schuster, F.; Sanchette, F. Effect of Nitrogen Content on Structural and Mechanical Properties of AlTiZrTaHf(-N) High Entropy Films Deposited by Reactive Magnetron Sputtering. *Surf. Coat. Technol.* **2022**, *432*, 128051. [[CrossRef](#)]
48. El Garah, M.; Touaibia, D.E.; Achache, S.; Michau, A.; Sviridova, E.; Postnikov, P.S.; Chehimi, M.M.; Schuster, F.; Sanchette, F. Data on Nitridation Effect of AlTiZrHf(-N) High Entropy Films by X-Ray Photoelectron Spectroscopy. *Data Brief* **2022**, *42*, 108241. [[CrossRef](#)] [[PubMed](#)]
49. Shi, J.; Muders, C.M.; Kumar, A.; Jiang, X.; Pei, Z.L.; Gong, J.; Sun, C. Study on Nanocomposite Ti–Al–Si–Cu–N Films with Various Si Contents Deposited by Cathodic Vacuum Arc Ion Plating. *Appl. Surf. Sci.* **2012**, *258*, 9642–9649. [[CrossRef](#)]
50. Lin, S.-Y.; Chang, S.-Y.; Huang, Y.-C.; Shieu, F.-S.; Yeh, J.-W. Mechanical Performance and Nanoindenting Deformation of (AlCrTaTiZr)NCy Multi-Component Coatings Co-Sputtered with Bias. *Surf. Coat. Technol.* **2012**, *206*, 5096–5102. [[CrossRef](#)]
51. Chang, S.-Y.; Lin, S.-Y.; Huang, Y.-C.; Wu, C.-L. Mechanical Properties, Deformation Behaviors and Interface Adhesion of (AlCrTaTiZr)Nx Multi-Component Coatings. *Surf. Coat. Technol.* **2010**, *204*, 3307–3314. [[CrossRef](#)]
52. Lai, C.-H.; Lin, S.-J.; Yeh, J.-W.; Chang, S.-Y. Preparation and Characterization of AlCrTaTiZr Multi-Element Nitride Coatings. *Surf. Coat. Technol.* **2006**, *201*, 3275–3280. [[CrossRef](#)]
53. Chang, H.-W.; Huang, P.-K.; Davison, A.; Yeh, J.-W.; Tsau, C.-H.; Yang, C.-C. Nitride Films Deposited from an Equimolar Al–Cr–Mo–Si–Ti Alloy Target by Reactive Direct Current Magnetron Sputtering. *Thin Solid Film.* **2008**, *516*, 6402–6408. [[CrossRef](#)]
54. Liang, S.-C.; Tsai, D.-C.; Chang, Z.-C.; Sung, H.-S.; Lin, Y.-C.; Yeh, Y.-J.; Deng, M.-J.; Shieu, F.-S. Structural and Mechanical Properties of Multi-Element (TiVCrZrHf)N Coatings by Reactive Magnetron Sputtering. *Appl. Surf. Sci.* **2011**, *258*, 399–403. [[CrossRef](#)]
55. Bouissil, A.; Achache, S.; Touaibia, D.E.; Panicaud, B.; Yazdi, M.A.P.; Sanchette, F.; El Garah, M. Properties of a New TiTaZrHfW(N) Refractory High Entropy Film Deposited by Reactive DC Pulsed Magnetron Sputtering. *Surf. Coat. Technol.* **2023**, *462*, 129503. [[CrossRef](#)]
56. Vepřek, S.; Reiprich, S.; Shizhi, L. Superhard Nanocrystalline Composite Materials: The TiN/Si₃N₄ System. *Appl. Phys. Lett.* **1995**, *66*, 2640–2642. [[CrossRef](#)]
57. Yashar, P.C.; Sproul, W.D. Nanometer Scale Multilayered Hard Coatings. *Vacuum* **1999**, *55*, 179–190. [[CrossRef](#)]
58. Sandu, C.S.; Sanjinés, R.; Benkahoul, M.; Medjani, F.; Lévy, F. Formation of Composite Ternary Nitride Thin Films by Magnetron Sputtering Co-Deposition. *Surf. Coat. Technol.* **2006**, *201*, 4083–4089. [[CrossRef](#)]
59. Muniz, F.T.L.; Miranda, M.A.R.; Morilla dos Santos, C.; Sasaki, J.M. The Scherrer Equation and the Dynamical Theory of X-Ray Diffraction. *Acta Crystallogr. Sect. A* **2016**, *72*, 385–390. [[CrossRef](#)]

60. Tsai, D.-C.; Chang, Z.-C.; Kuo, B.-H.; Shiao, M.-H.; Chang, S.-Y.; Shieu, F.-S. Structural Morphology and Characterization of (AlCrMoTaTi)N Coating Deposited via Magnetron Sputtering. *Appl. Surf. Sci.* **2013**, *282*, 789–797. [[CrossRef](#)]
61. Nieborek, M.; Jastrzębski, C.; Płociński, T.; Wróbel, P.; Seweryn, A.; Judek, J. Optimization of the Plasmonic Properties of Titanium Nitride Films Sputtered at Room Temperature through Microstructure and Thickness Control. *Sci. Rep.* **2024**, *14*, 5762. [[CrossRef](#)]
62. Rost, C.M.; Sachet, E.; Borman, T.; Moballeggh, A.; Dickey, E.C.; Hou, D.; Jones, J.L.; Curtarolo, S.; Maria, J.-P. Entropy-Stabilized Oxides. *Nat. Commun.* **2015**, *6*, 8485. [[CrossRef](#)]
63. Patscheider, J.; Zehnder, T.; Diserens, M. Structure–Performance Relations in Nanocomposite Coatings. *Surf. Coat. Technol.* **2001**, *146–147*, 201–208. [[CrossRef](#)]
64. Chen, Y.-H.; Lee, K.W.; Chiou, W.-A.; Chung, Y.-W.; Keer, L.M. Synthesis and Structure of Smooth, Superhard TiN/SiN_x Multilayer Coatings with an Equiaxed Microstructure. *Surf. Coat. Technol.* **2001**, *146–147*, 209–214. [[CrossRef](#)]
65. Hu, X.; Zhang, H.; Dai, J.; Li, G.; Gu, M. Study on the Superhardness Mechanism of Ti–Si–N Nanocomposite Films: Influence of the Thickness of the Si₃N₄ Interfacial Phase. *J. Vac. Sci. Technol. A* **2004**, *23*, 114–117. [[CrossRef](#)]
66. Dong, Y.; Zhao, W.; Yue, J.; Li, G. Crystallization of Si₃N₄ Layers and Its Influences on the Microstructure and Mechanical Properties of ZrN/Si₃N₄ Nanomultilayers. *Appl. Phys. Lett.* **2006**, *89*, 121916. [[CrossRef](#)]
67. Xu, J.; Hattori, K.; Seino, Y.; Kojima, I. Microstructure and Properties of CrN/Si₃N₄ Nano-Structured Multilayer Films. *Thin Solid Film.* **2002**, *414*, 239–245. [[CrossRef](#)]
68. Jeong, J.J.; Hwang, S.K.; Lee, C. Hardness and Adhesion Properties of HfN/Si₃N₄ and NbN/Si₃N₄ Multilayer Coatings. *Mater. Chem. Phys.* **2003**, *77*, 27–33. [[CrossRef](#)]
69. Jeong, J.J.; Lee, C.M. Effects of Post-Deposition Annealing on the Mechanical and Chemical Properties of the Si₃N₄/NbN Multilayer Coatings. *Appl. Surf. Sci.* **2003**, *214*, 11–19. [[CrossRef](#)]
70. Parry, V. *Corrosion Sèche Des Métaux—Méthodes D'étude*; Techniques de l'Ingénieur: Saint-Denis, France, 2015. [[CrossRef](#)]
71. Gorr, B.; Mueller, F.; Christ, H.-J.; Mueller, T.; Chen, H.; Kauffmann, A.; Heilmaier, M. High Temperature Oxidation Behavior of an Equimolar Refractory Metal-Based Alloy 20Nb20Mo20Cr20Ti20Al with and without Si Addition. *J. Alloys Compd.* **2016**, *688*, 468–477. [[CrossRef](#)]
72. Antoni, L.; Galerie, A. Corrosion sèche des métaux—Mécanismes. *Corros. Vieil.* **2003**. [[CrossRef](#)]
73. Hung, S.-B.; Wang, C.-J.; Chen, Y.-Y.; Lee, J.-W.; Li, C.-L. Thermal and Corrosion Properties of V-Nb-Mo-Ta-W and V-Nb-Mo-Ta-W-Cr-B High Entropy Alloy Coatings. *Surf. Coat. Technol.* **2019**, *375*, 802–809. [[CrossRef](#)]
74. Gorr, B.; Schellert, S.; Müller, F.; Christ, H.-J.; Kauffmann, A.; Heilmaier, M. Current Status of Research on the Oxidation Behavior of Refractory High Entropy Alloys. *Adv. Eng. Mater.* **2021**, *23*, 2001047. [[CrossRef](#)]
75. Li, S.; Yamaguchi, T. High-Temperature Oxidation Behavior of Laser-Cladded Refractory NiSi_{0.5}CrCoMoNb_{0.75} High-Entropy Coating. *J. Mater. Res. Technol.* **2022**, *17*, 1616–1627. [[CrossRef](#)]
76. Logan, S.R. The Origin and Status of the Arrhenius Equation. *J. Chem. Educ.* **1982**, *59*, 279. [[CrossRef](#)]
77. Schmitt, T. Mécanismes de Dégradation de Revêtements Base CrN Élaborés Par Arc-PVD: Intérêt D'une Nano-Architecture. Ph.D. Thesis, Ecole Centrale de Lyon, Écully, France, 2010.
78. Kumar, P.; Avasthi, S. Diffusion Barrier with 30-Fold Improved Performance Using AlCrTaTiZrN High-Entropy Alloy. *J. Alloys Compd.* **2020**, *814*, 151755. [[CrossRef](#)]
79. Chu, T.L.; Lee, C.H.; Gruber, G.A. The Preparation and Properties of Amorphous Silicon Nitride Films. *J. Electrochem. Soc.* **1967**, *114*, 717. [[CrossRef](#)]
80. Tien, T.Y.; Bonnel, D.A. *Preparation and Properties of Silicon Nitride Based Materials*; Trans Tech Publications Ltd.: Baech, Switzerland, 1989; ISBN 978-3-0357-0445-7.
81. Hovsepian, P.E.; Lewis, D.B.; Münz, W.-D. Recent Progress in Large Scale Manufacturing of Multilayer/Superlattice Hard Coatings. *Surf. Coat. Technol.* **2000**, *133–134*, 166–175. [[CrossRef](#)]
82. Tomlinson, M.; Lyon, S.B.; Hovsepian, P.; Munz, W.-D. Corrosion Performance of CrN/NbN Superlattice Coatings Deposited by the Combined Cathodic Arc/Unbalanced Magnetron Technique. *Vacuum* **1999**, *53*, 117–121. [[CrossRef](#)]
83. Zhang, W.; Liao, J.J.; Yang, Z.B.; Qiu, S.Y.; Yang, J.J.; Liao, J.L.; Yang, Y.Y.; Liu, N. Improved Corrosion Resistance of Reactive Gas Pulse Sputtered (TiTa NbZrNi)N High Entropy Alloy Coatings with a Hybrid Architecture of Multilayered and Compositionally Graded Structures. *J. Nucl. Mater.* **2021**, *543*, 152558. [[CrossRef](#)]
84. Steyer, P.; Pilloud, D.; Pierson, J.F.; Millet, J.-P.; Charnay, M.; Stauder, B.; Jacquot, P. Oxidation Resistance Improvement of Arc-Evaporated TiN Hard Coatings by Silicon Addition. *Surf. Coat. Technol.* **2006**, *201*, 4158–4162. [[CrossRef](#)]

Disclaimer/Publisher's Note: The statements, opinions and data contained in all publications are solely those of the individual author(s) and contributor(s) and not of MDPI and/or the editor(s). MDPI and/or the editor(s) disclaim responsibility for any injury to people or property resulting from any ideas, methods, instructions or products referred to in the content.